nature physics

Article

https://doi.org/10.1038/s41567-024-02469-1

# Boundary modes of a charge density wave state in a topological material

Received: 1 February 2023

Accepted: 7 March 2024

Published online: 7 June 2024

Check for updates

Maksim Litskevich[1,18], Md Shafayat Hossain[1,18] ✉, Song-Bo Zhang[2,3,4,18], Zi-Jia Cheng[1], Satya N. Guin[5,6], Nitesh Kumar[5,7], Chandra Shekhar[5], Zhiwei Wang[8,9,10], Yongkai Li[8,9,10], Guoqing Chang[11], Jia-Xin Yin[1], Qi Zhang[1], Guangming Cheng[12], Tyler A. Cochran[1], Nana Shumiya[1], Yu-Xiao Jiang[1], Xian P. Yang[1], Daniel Multer[1], Xiaoxiong Liu[4,13,14,15,16], Nan Yao[12], Yugui Yao[8,9], Claudia Felser[5], Titus Neupert[4] & M. Zahid Hasan[1,17] ✉

Charge density waves appear in numerous condensed matter platforms ranging from high-temperature superconductors to quantum Hall systems. Despite such ubiquity, there has been a lack of direct experimental study of boundary states that can uniquely stem from the charge order. Here we directly visualize the bulk and boundary phenomenology of the charge density wave in a topological material, $Ta_2Se_8I$, using scanning tunnelling microscopy. At a monolayer step edge, we demonstrate the presence of an in-gap boundary mode persisting up to the charge ordering temperature with modulations along the edge that match the charge density wave wavevector along the edge. Furthermore, these results manifesting the presence of an edge state challenge the existing axion insulator interpretation of the charge-ordered phase in this compound.

Axion particles, originally proposed as an explanation for the absence of charge–parity violation in the strong interaction between quarks and as a candidate for dark matter, found their manifestation in condensed matter platforms such as topological antiferromagnets, ferromagnetic topological insulators and charge density wave Weyl semimetals[1–10]. $Ta_2Se_8I$ is the only known material platform so far[11–14] where, in theory, a charge density wave transition from a Weyl semimetal state could lead to an axion insulator phase. Here, the charge density wave, whose sliding mode (phason) is an axion, supposedly connects the pair of Weyl points with opposite chirality at different positions in the momentum space, thus breaking the chiral symmetry of the Weyl semimetal, opening an insulating gap (Fig. 1a) and tentatively realizing an axion insulator. An axion insulator features (1) a quantized, bulk magnetoelectric coupling coefficient of $\pi$ (refs. 15–17) that is challenging to access experimentally and (2) a gapless, time-reversal symmetry protected topological surface state[12] that is readily accessible

[1]Laboratory for Topological Quantum Matter and Advanced Spectroscopy (B7), Department of Physics, Princeton University, Princeton, NJ, USA. [2]Hefei National Laboratory, Hefei, China. [3]International Center for Quantum Design of Functional Materials, University of Science and Technology of China, Hefei, China. [4]Department of Physics, University of Zurich, Zurich, Switzerland. [5]Max Planck Institute for Chemical Physics of Solids, Dresden, Germany. [6]Department of Chemistry, Birla Institute of Technology and Science, Hyderabad, India. [7]S. N. Bose National Centre for Basic Sciences, Salt Lake City, India. [8]Centre for Quantum Physics, Key Laboratory of Advanced Optoelectronic Quantum Architecture and Measurement (MOE), School of Physics, Beijing Institute of Technology, Beijing, China. [9]Beijing Key Lab of Nanophotonics and Ultrafine Optoelectronic Systems, Beijing Institute of Technology, Beijing, China. [10]Material Science Center, Yangtze Delta Region Academy of Beijing Institute of Technology, Jiaxing, China. [11]Division of Physics and Applied Physics, School of Physical and Mathematical Sciences, Nanyang Technological University, Singapore, Singapore. [12]Princeton Materials Institute, Princeton University, Princeton, NJ, USA. [13]Shenzhen Institute for Quantum Science and Engineering and Department of Physics, Southern University of Science and Technology, Shenzhen, China. [14]Quantum Science Center of Guangdong-Hong Kong-Macao Greater Bay Area (Guangdong), Shenzhen, China. [15]Shenzhen Key Laboratory of Quantum Science and Engineering, Shenzhen, China. [16]International Quantum Academy, Shenzhen, China. [17]Quantum Science Center (QSC, ORNL), Oak Ridge, TN, USA. [18]These authors contributed equally: Maksim Litskevich, Md Shafayat Hossain, Song-Bo Zhang. ✉e-mail: mdsh@princeton.edu; mzhasan@princeton.edu

https://doi.org/10.1038/s41567-024-02469-1

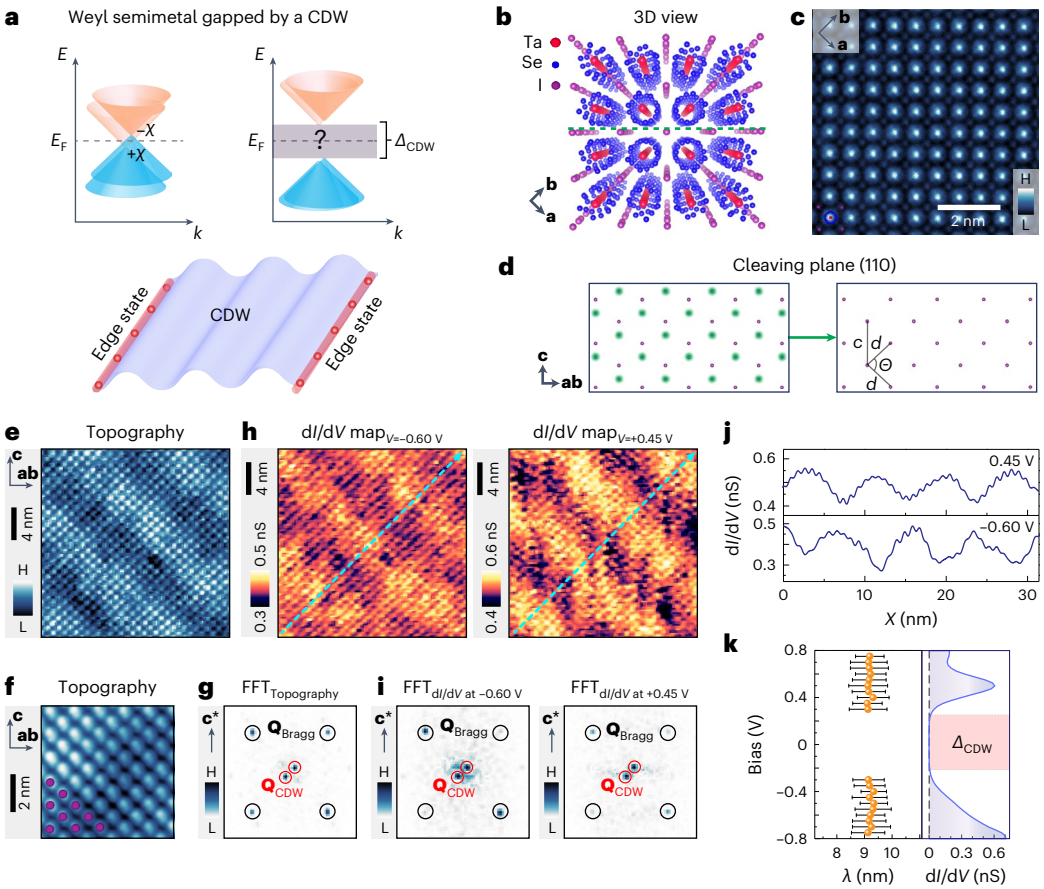


**Fig. 1 | Electronic nature of charge density wave in $Ta_2Se_8I$. a**, Top: a schematic of the phase transition from a Weyl semimetal (with two Weyl cones of opposite chirality $+\chi$ and $-\chi$) into a charge density wave insulator[13]. Chiral crystals have, in general, pairs of Weyl fermions located at different energies[59]. Bottom: a real space representation of an edge state residing within the insulating charge density wave gap. Edge modes and edge-localized electrons are illustrated using red lines and dots, respectively. **b**, Three-dimensional view of the crystal structure of $Ta_2Se_8I$. The dashed green line marks the cleaving plane. **c**, A STEM image within the **ab** plane. H and L labels in the colour bar denote high and low scale, respectively. **d**, Left: a schematic of the (110) cleaving plane containing iodine atoms (denoted with green shadows). Note that **ab** ∥ (**a** + **b**). Right: the resulting cleaving plane after 50% of iodine atoms are removed. Interatomic distances ($d \approx 9.5$ Å, $c \approx 13$ Å, $\Theta \approx 86 \pm 0.5°$) are marked. **e**, A topographic image of the (110) plane exhibiting a charge density wave with $\lambda_{CDW} = 9.1 \pm 0.6$ nm ($V_{gap} = -1.0$ V, $I_t = 50$ pA). H and L labels in the colour bar denote high and low scale, respectively. **f**, An enlarged view of the topographic image showing a clear lattice of iodine atoms. **g**, The Fast Fourier transform of the topographic image in **e**, displaying a well-developed charge density wave ($\mathbf{Q}_{CDW}$) and Bragg ($\mathbf{Q}_{Bragg}$) peaks. **h**, d*I*/d*V* maps ($V_{gap} = -0.60$ V (left) and 0.45 V (right), $I_t = 0.3$ nA, $V_{mod} = 10$ mV) demonstrating a reversal of the spectroscopic contrast of the charge density wave as the tip–sample bias is tuned from the valence to the conduction band. **i**, The Fourier transforms of the d*I*/d*V* maps in **h**, showcasing the charge density wave peaks. **j**, d*I*/d*V* line profiles derived from linecuts (marked with cyan lines in **h**) at distance *X* along the $\mathbf{Q}_{CDW}$ direction, showcasing a spectroscopic contrast inversion. **k**, Left: the energy dependence of the wavelength of the charge density wave derived from d*I*/d*V* maps. Data points are presented as ($\lambda \pm \delta\lambda$); the wavelength ($\lambda$) and its uncertainty ($\delta\lambda$) are extracted from the location and the width of the $\mathbf{Q}_{CDW}$ peak in the FFT of the d*I*/d*V* maps. Right: the averaged differential spectrum, replicated from Supplementary Fig. 4b, showcasing a large insulating gap. The dashed vertical line indicates zero differential conductance. The data in **e**–**k** were taken at $T = 160$ K.

in spectroscopic techniques. Still, the topology of the charge density wave insulator phase of $Ta_2Se_8I$ remains unknown and subject to debate[4,5,11–14,18]. In this Article, employing scanning tunnelling microscopy, we uncover a boundary mode (edge state) residing within the bulk charge density wave gap and unveil an intimate connection between the edge mode and the charge-ordered state. Notably, we also find that there is no detectable surface state present within the charge density wave[19]. This is incompatible with the prevailing assumption of an axion insulator ground state in $Ta_2Se_8I$, which must carry a surface Dirac cone in a non-magnetic material. Taken together, these observations hint at a unique nature of the charge density wave state, different from an axion insulator.

$Ta_2Se_8I$ has a quasi-one-dimensional crystal structure with Ta and I atomic chains running along the *c* axis of the crystal (Fig. 1b). Ta atoms form strong covalent bonds with adjacent Se atoms, whereas I atoms are weakly tied to Ta–Se chiral chains. $Ta_2Se_8I$ crystals grow in a few-millimetre-long needle shape with an aspect ratio of approximately 10, reflecting its one-dimensional nature (see Fig. 1c, inset and Methods for details on the crystal growth). Scanning transmission electron microscopy (STEM) perpendicular to the growth direction (*c*) reveals a squared arrangement of Ta and I atoms (Fig. 1c). Due to a weak interaction of I atoms with Ta–Se chains, $Ta_2Se_8I$ has a natural cleaving plane (110) as marked in Fig. 1b. Using STEM and electron diffraction analysis, we confirm that the cleaving plane of our samples is (110) (see Methods and Supplementary Fig. 1 for details). We cleave $Ta_2Se_8I$ samples in situ in ultrahigh vacuum conditions ($<5 \times 10^{-10}$ mbar) for our scanning tunnelling microscopy measurements. In the scanning tunnelling microscopy image on a clean, freshly cleaved sample, we find that the surface contains I atoms, 50% of which are expelled from the original honeycomb-like lattice (Fig. 1d), leaving a close-to-squared I lattice with the following interatomic distances (marked in Fig. 1d, right): $d \approx 9.5$ Å, $c \approx 13$ Å, $\Theta \approx 86 \pm 0.5°$ (Fig. 1e,f); this is consistent with the prior

scanning tunnelling microscopy data[20,21]. Notably, the topography taken at $T = 160$ K visualizes a one-dimensional charge density wave (Fig. 1e). The Fourier transform of the large-scale drift corrected topography[22] image reveals Bragg peaks with a close-to-squared lattice symmetry, as well as the charge density wave wavevector peaks (Fig. 1g). We determine the charge density wave period, $\lambda_{CDW}$, to be $9.1 \pm 0.6$ nm. The charge density wave wavevector, $\mathbf{Q}_{CDW} \approx \left(0.054\frac{2\pi}{a}, -0.054\frac{2\pi}{a}, 0.098\frac{2\pi}{c}\right)$ lies in the (110) plane (see Supplementary Information and Supplementary Figs. 2 and 3 for details). While the charge density wave wavelength remains relatively uniform within a single batch of samples, it shows slight variations across samples from different batches, averaging at $\overline{\lambda_{CDW}} = 10.4 \pm 1.6$ nm. Our result is consistent with X-ray and neutron scattering experiments[23–29] but differs slightly from recent scanning tunnelling microscopy data that report an enlarged $\lambda_{CDW} = 17 \pm 1$ nm attributed to the growth condition and doping effect of abundant I vacancies[20,21].

Having explored the crystal structure of $Ta_2Se_8I$, we focus on tunnelling spectroscopy measurements. First, we show two d$I$/d$V$ spectroscopic maps, taken at the same location at −0.60 V and 0.45 V, in Fig. 1h. The d$I$/d$V$ maps crucially reveal that the local density of states maxima at 0.45 V corresponds to the local density of states minima at −0.60 V, signifying a spectroscopic contrast reversal upon adjusting the tip–sample bias from the conduction band to the valence band (Fig. 1j). This contrast switch is typically associated with the electronic character of the charge order[30–32]. The Fourier transform images of the spectroscopic maps in Fig. 1h, illustrated in Fig. 1i, unambiguously reveal the presence of long-wavelength charge density wave peaks that align well with the corresponding peaks from topography. Next, we turn to energy-resolved d$I$/d$V$ spectroscopy. It is first worth emphasizing that, as shown in Fig. 1k (left), $\lambda_{CDW}$ remains constant across varying energy levels, a behaviour anticipated from a charge density wave state. At $T = 160$ K, spatially resolved differential spectra taken on the atomic, defect-free surface reveal a large insulating gap (Supplementary Fig. 4b; see Supplementary Information and Supplementary Fig. 5 for the details on energy gap determination). Analysing the average d$I$/d$V$ spectrum, we find the energy gap, $\Delta_{CDW}$ to be ~550 meV (Fig. 1k, right and Supplementary Fig. 4b). It is worth comparing our $\Delta_{CDW}$ with the gaps obtained from other techniques. The energy difference between the Fermi level and valence band in our tunnelling spectra is ~260 meV, which matches well with our photoemission spectroscopy data (see Methods and Supplementary Fig. 6 for details), where the energy difference between the Fermi energy and the emergence of spectral weight density below the Fermi level is ~250 meV. These values are consistent with previous photoemission spectroscopy experiments[14,20,33]. On the other hand, our tunnelling $\Delta_{CDW}$ appears to be larger than the gap observed in transport measurements[5,20] and recent scanning tunnelling microscopy data[21]; it is possible that the crystal defects and numerous I vacancies (that manifest through a larger $\lambda_{CDW}$) in their sample can cause the discrepancy between the results (see Supplementary Information for details). To investigate the origin of the large energy gap, we compare our experimental results with the outcomes of the mean-field theory of a charge density wave[34]. The mean-field formula that relates the magnitude of the charge density wave gap and the transition temperature assuming weak coupling is $\Delta_{CDW}/3.52k_BT_{CDW} = 1$. Note that it has a direct analogy to the Bardeen–Cooper–Schrieffer theory of superconductivity[34]. Here, in $Ta_2Se_8I$, however, $\Delta_{CDW}/3.52k_BT_{CDW} \approx 7$ ($\Delta_{CDW} \approx 550$ meV, $T_{CDW} \approx 260$ K) is nearly an order of magnitude larger than what is expected from a traditional, weak coupling charge density wave. This indicates the presence of strong coupling in the charge density wave state of $Ta_2Se_8I$ (refs. 35,36). In the context of the large $\Delta_{CDW}$, it is worth noting that our observation of a substantial insulating energy gap in the surface, accompanied by the absence of discernible in-gap d$I$/d$V$ intensity, indicates the absence of surface states in the time-reversal symmetric material $Ta_2Se_8I$. Our photoemission spectroscopy data support this absence (Supplementary Fig. 6). As discussed above, this observation contradicts the existence of the axion insulator state in $Ta_2Se_8I$. Furthermore, the energy scale of the spin–orbit coupling, which determines the energy window of the Weyl physics and the energy gap of an axion insulator, is approximately $\Delta_{SO} \approx 20$ meV in $Ta_2Se_8I$ (ref. 37). This value is substantially smaller than the observed $\Delta_{CDW}$. The substantial difference in energy scales between the axion insulator and $\Delta_{CDW}$ strongly suggests that the axion insulator state is highly improbable in $Ta_2Se_8I$.

We further investigate the large charge density wave gap by examining its spatial dependence. While the magnitude of the tunnelling spectra is dependent on both tip and sample, the energy gap usually correlates with the electronic nature of the sample only. In our case, spatially resolved tunnelling spectra taken along the charge density wavevector direction reveal a spatially modulated energy gap with a modulation amplitude of ~40 meV and periodicity of ~$12 \pm 1$ nm (Supplementary Fig. 4a–c). This periodicity closely matches the charge density wave period of the specific sample, which has been extracted from topography. Moreover, comparing the topography and the spatial dependence of the charge density wave gap, we find that the topographic maxima (minima) correspond to the gap minima (maxima). Such a spatial gap modulation associated with the charge density wave has been seen in several charge density wave compounds[30,38] and interpreted as evidence for the electronic nature of the charge density wave. Taken collectively, our observations of direct correlations between (1) the charge density wave in topography, (2) charge density wave wavevector peaks in the Fourier transform of the spectroscopic map and (3) the spatially modulated charge density wave gap, alongside the demonstrated spectroscopic contrast reversal upon altering the tip–sample bias from the conduction band to the valence band, all consistently support the electronic nature for the charge density wave in $Ta_2Se_8I$.

Having discussed the electronic nature of the charge density wave in $Ta_2Se_8I$, we investigate the topological properties of the charge density wave state. Figure 2 captures the highlight of our experiment—the observation of an in-gap edge state within the charge density wave. The scanning tunnelling microscopy topography image in Fig. 2a illustrates an atomically sharp monolayer step edge along the $c$ direction (see Supplementary Fig. 1 for an analysis of edge orientations). The height line profile perpendicular to the edge clearly shows uniform atomic correlations on the two sides of the monolayer step edge (Fig. 2b). The phase of the charge density wave appears to be continuous across the edge, consistent with the bulk nature (not from trivial surface effects) of the charge density wave (see Supplementary Information and Supplementary Fig. 3 for more details). To probe the electronic states localized at the edge, we perform d$I$/d$V$ measurements along the line (Fig. 2a) passing through the edge. Away from the edge, the tunnelling spectra feature a large insulating gap (Fig. 2c, blue curves). In sharp contrast, the spectra taken at the edge (Fig. 2c, orange curves) reveal a pronounced finite density of states within the insulating gap. The presence of the in-gap state localized at the edge suggests the existence of edge modes[39–55] in the charge density wave phase of $Ta_2Se_8I$.

To further explore the edge state, in Fig. 2d we show d$I$/d$V$ spectroscopic maps taken at a monolayer step edge identified by a topographic image (Fig. 2d, bottom). In the real-space differential conductance maps at the Fermi level and $E = \pm 100$ meV, we find that the monolayer step edge exhibits pronounced edge states manifested via increased differential conductance within the insulating gap. In contrast, the spectroscopic image at −0.8 V (Fig. 2d, top) exhibits suppressed differential conductance along the edge. Figure 2e, which depicts the spatial spread of the edge state, reveals an exponential decay of the edge state on the crystal side of the step edge. The edge state decays with a characteristic length of $r_0 \approx 1.25$ nm on the crystal side, indicating a strongly confined nature of the edge state. Note that this is nearly 50 times smaller than in HgTe/CdTe quantum wells and 2 times larger than in bismuthene[39,43,55]. The strongly confined nature of the edge state

https://doi.org/10.1038/s41567-024-02469-1

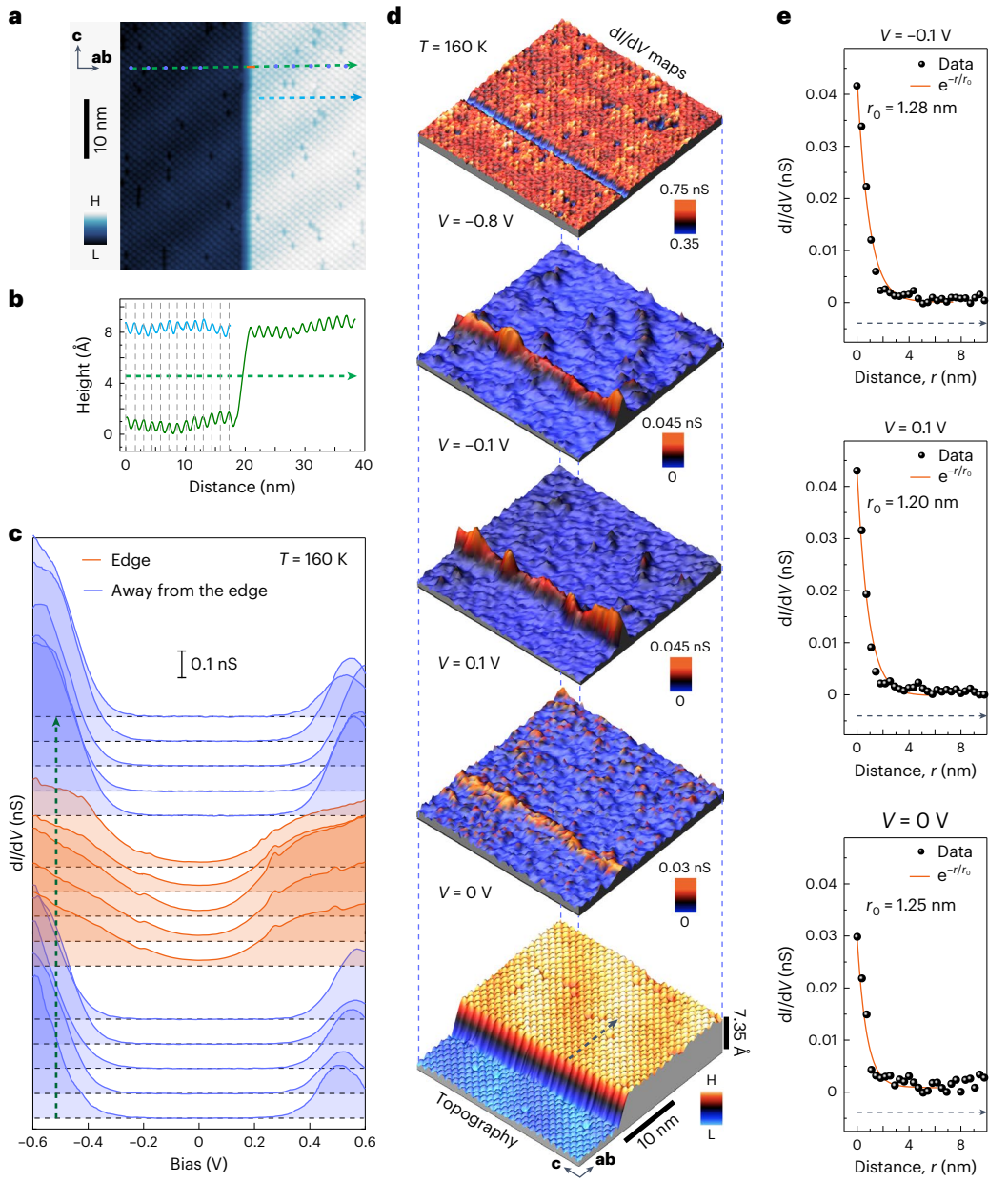


**Fig. 2 | Observation of an edge state within the charge density wave gap.** **a**, Atomically resolved topography of an atomically sharp monolayer step edge ($V_{gap}$ = −1.0 V, $I_t$ = 50 pA). H and L labels in the colour bar denote high and low scale, respectively. **b**, The corresponding height profile, taken perpendicular to the *c*-axis direction, exhibits uniform atomic correlations perpendicular to the step edge over a large distance. The vertical dashed lines denote the atomic positions perpendicular to the *c* axis. **c**, Tunnelling spectroscopy taken at *T* = 160 K, revealing an insulating gap away from the edge and a pronounced in-gap state on the edge. The orange and blue curves represent the differential spectra taken at different positions (marked in **a**) with the direction indicated by the green arrow in **a** and **c**) at the edge and away from the edge, respectively. Spectra are offset for clarity. Dashed horizontal lines denote zero differential conductance. The tunnelling junction set-up is $V_{set}$ = −0.8 V, $I_{set}$ = 0.4 nA and $V_{mod}$ = 10 mV. **d**, d*I*/d*V* maps taken at 160 K at different bias voltages (the corresponding topography is shown at the bottom). d*I*/d*V* maps taken within the insulating gap (*V* = 0 mV and ±100 mV) reveal a pronounced in-gap edge state. The tunnelling junction set-up for the d*I*/d*V* maps is $V_{set}$ = −0.8 V, $I_{set}$ = 0.3 nA and $V_{mod}$ = 10 mV. **e**, The intensity distribution of differential conductance taken at 0 and ±100 mV away from the step edge on the crystal side. The corresponding location is marked on the topographic image in **d** with a black dashed line; the direction is marked with an arrow. The orange curves show the exponential fitting of the decay of the state away from the edge.

is evident in Supplementary Fig. 7, displaying line profiles for the topography and corresponding d*I*/d*V* around the step edge. These profiles illustrate that the edge state exhibits exponential localization within the crystal side, diminishing as it extends towards the vacuum side.

With the electronic nature and the edge states associated with the charge density wave insulator phase in $Ta_2Se_8I$ now addressed, we shift our focus to its temperature dependence. In Fig. 3a, we show large-scale topography images and the corresponding Fourier transforms (inset) at 160, 250 and 280 K. The charge density wave and the corresponding Fourier transform peaks are detected in the 160 and 250 K topography images. On the other hand, neither the charge density wave nor its Fourier transform peaks are seen in the 280 K data (Fig. 3a, right). This observation is consistent with recent scanning tunnelling microscopy data[21] and is corroborated by our transport measurement shown in Fig. 3b, which indicates that the charge density wave transition occurs at $T_{CDW} \approx 260$ K (refs. 5,23–29). The charge density wave transition also

https://doi.org/10.1038/s41567-024-02469-1

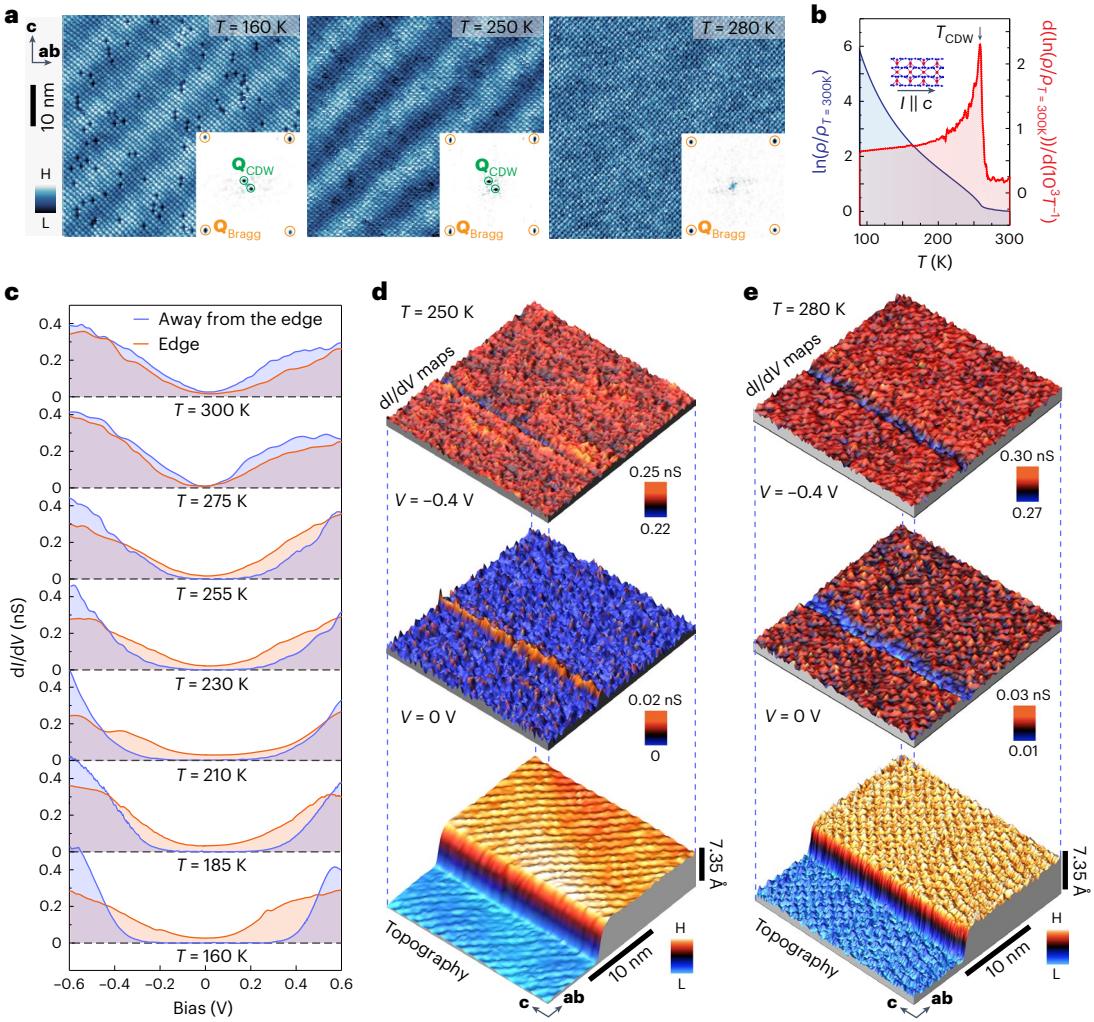


**Fig. 3 | Temperature dependence of the charge density wave and its in-gap edge state. a**, Topography images and corresponding Fourier transforms (inset) taken at three different temperatures, highlighting the temperature evolution of the charge density wave ($V_{gap}$ = −1.0 V, $I_t$ = 50 pA). H and L labels in the colour bar denote high and low scale, respectively. At $T$ = 280 K, the charge density wave and its Fourier transform peaks are not detected. $\mathbf{Q}_{CDW}$ and $\mathbf{Q}_{Bragg}$ denote the charge density wave and Bragg peaks, respectively. **b**, Resistivity versus temperature data (with current, $I$, flowing along the $c$ axis of the crystal) showing a kink near 260 K signalling the charge density wave transition, which corroborates our observation. The red curve represents the plot of the derivative of the natural logarithm of the ratio of $\rho$ to $\rho_{T=300K}$ with respect to $\frac{10^3}{T}$. **c**, Temperature-dependent differential spectra taken at the edge and away from the edge, denoted with orange and blue curves, respectively. Spectra are offset for clarity for different temperatures. In agreement with the topography, the charge density wave gap and the associated in-gap edge state are not visible above the transition temperature. The tunnelling junction set-up is $V_{set}$ = −0.8 V, $I_{set}$ = 0.4 nA and $V_{mod}$ = 10 mV. **d**,**e**, Topography and corresponding differential conductance maps taken on a monolayer step edge at $T$ = 250 K (**d**) and 280 K (**e**), capturing the temperature dependence of the edge state. At $T$ = 250 K, the edge state is still visible, whereas at $T$ = 280 K, the edge state is absent. The tunnelling junction set-up for d$I$/d$V$ maps is $V_{set}$ = −0.8 V, $I_{set}$ = 0.3 nA and $V_{mod}$ = 10 mV.

manifests in our temperature-dependent tunnelling spectra presented in Fig. 3c. The insulating gap shrinks progressively as we raise the temperature, and finally a semi-metallic behaviour is seen at 280 K (Fig. 3c, blue curves). Concurrently, tunnelling spectra taken at a monolayer step edge (Fig. 3c, orange curves) show that the in-gap edge state, which has an enhanced d$I$/d$V$ within the insulating gap, is present throughout the range of temperatures below $T_{CDW}$. However, above $T_{CDW}$, the d$I$/d$V$ spectrum at the edge is suppressed compared with the d$I$/d$V$ spectrum away from the edge, signalling the absence of the edge state in the semimetal phase of $Ta_2Se_8I$. We further substantiate this observation by acquiring spectroscopic maps as the transition temperature is crossed (Fig. 3d,e). At 250 K, a pronounced in-gap localized state is present at the edge, whereas at 280 K, the d$I$/d$V$ at the edge is rather suppressed. These results are in accordance with a transition from the charge density wave insulator to the Weyl semimetal phase. It is worth noting that the Weyl physics in $Ta_2Se_8I$ exists within a narrow energy window, on the order of $\lesssim$20 meV, which is substantially smaller than the charge density wave gap (~500 meV). Furthermore, as demonstrated in our experiments and corroborated by our theoretical analysis below, the localization length of the edge state varies inversely with the charge density wave gap and is expected to diverge as the charge density wave gap closes in the Weyl semimetal phase (Supplementary Fig. 8). Consequently, it is highly improbable that the Weyl physics plays a relevant role in the existence of the edge state.

The temperature dependence reveals that the edge state is quite robust and vanishes as soon as the charge density wave gap closes above $T_{CDW}$, suggesting its connection to the charge density wave insulating gap. To gain deeper insights into the relationship between the edge state and the charge density wave, we focus on a monolayer step edge, conducting comprehensive spectroscopic mapping as summarized in Fig. 4. In Fig. 4a, we show the topography and corresponding representative differential conductance maps around a monolayer step

https://doi.org/10.1038/s41567-024-02469-1

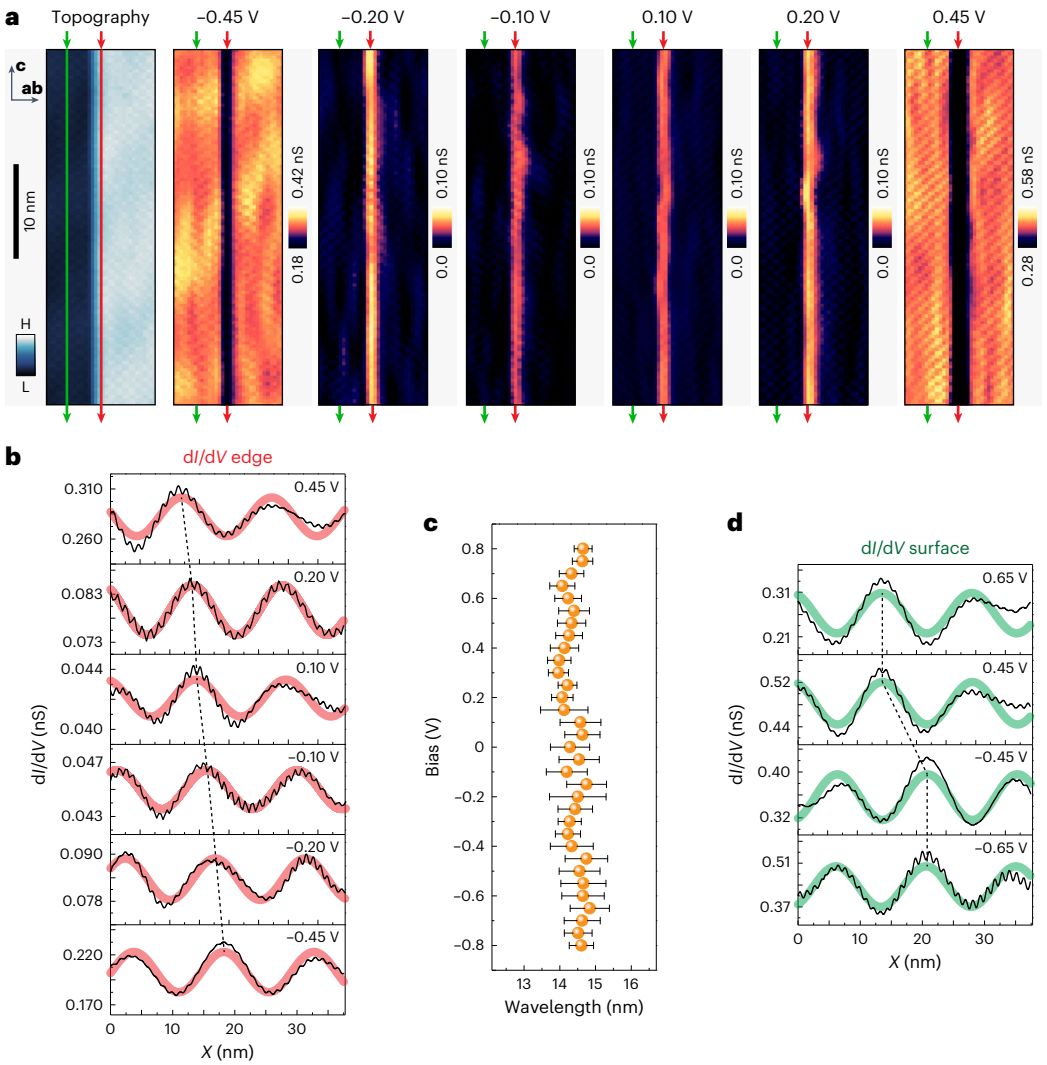


**Fig. 4 | Correspondence between the periodicity of the edge d*I*/d*V* modulations and charge density wave wavelength projected along the edge.** **a**, Topography and corresponding representative d*I*/d*V* maps around a monolayer step edge, revealing an in-gap edge state. H and L labels in the colour bar denote high and low scale, respectively. The red and green arrows indicate the location of the edge in the *ab* axis and the location on the surface where the line profiles presented in **d** were taken, respectively. The tunnelling junction set-up for d*I*/d*V* maps is $V_{set} = -0.8$ V, $I_{set} = 0.3$ nA and $V_{mod} = 10$ mV. All data were taken at $T = 160$ K. The charge density wave in this specific sample exhibits a periodicity of $\lambda_{CDW} = 10.1 \pm 0.3$ nm, deduced from topographic imaging of a region located away from the edge. **b**, d*I*/d*V* line profiles (averaged over an atom along the edge marked with a red vertical line in the topographic image in **a**) along the edge for six biases, exhibiting a periodic modulation fitted with $A \sin \frac{2\pi}{\lambda}(x - \phi)$; fitting parameters are $\lambda$ and $\phi$, which denote wavelength and phase shift, respectively. Averaging $\lambda$ obtained from the fitted sinusoids of all such acquired d*I*/d*V* curves, we obtain $\lambda_{avg} = 14.4 \pm 0.7$ nm. The red curves denote fitting of $A \sin \frac{2\pi}{\lambda_{avg}}(x - \phi)$ applied to d*I*/d*V* data at each bias. **c**, The deduced periodicity ($\lambda$) of the edge d*I*/d*V* oscillations plotted against the bias, highlighting an energy-independent $\lambda$ and consequent wavevector. Data points are presented as $(\lambda \pm \delta\lambda)$, where $\lambda$ and $\delta\lambda$ denote the optimal fitting parameter and its 95% confidence interval, respectively. Note that $\lambda_{avg}$ aligns well with the charge density wave wavelength projected along the edge, that is, $\sqrt{2}\lambda_{CDW}$. **d**, d*I*/d*V* line profiles (averaged over an atom along the *c*-axis direction marked with a vertical green line in the topographic image in **a**) away from the edge shown for four biases, exhibiting a periodic modulation fitted with $A \sin \frac{2\pi}{\lambda}(x - \phi)$; the fitting parameters are $\lambda$ and $\phi$, which denote the wavelength and phase shift, respectively. Averaging $\lambda$ obtained from the fitted sinusoids of all such d*I*/d*V* curves, we obtain $\lambda_{avg} = 14.2 \pm 0.6$ nm. The green curves denote the fitting of $A \sin \frac{2\pi}{\lambda_{avg}}(x - \phi)$ applied to the d*I*/d*V* data at each bias. Dashed black lines in **b** and **d** trace a shift of the d*I*/d*V* peak location upon varying the voltage bias.

edge, acquired at various bias voltages, unveiling the presence of an in-gap edge state. d*I*/d*V* line profiles along the edge extracted from these spectroscopic maps reveal a periodic modulation with a periodicity of $\lambda_{avg} = 14.4 \pm 0.7$ nm (Fig. 4b,c), equivalent to $(1.43 \pm 0.07)\lambda_{CDW}$ (where $\lambda_{CDW}$ is obtained from the topography), closely matching the charge density wave period projected along the edge ($\sqrt{2}\lambda_{CDW}$). This correspondence provides robust evidence of a connection between the edge state and the charge order. Notably, the periodicity of the in-gap edge d*I*/d*V* oscillations and consequently the associated wavevector obtained through a Fourier transform remains unaltered with energy (Fig. 4c). Intriguingly, however, the phase of the charge order, $\phi$, gradually shifts with energy, which is readily apparent through the discernible shifts in the positions of the d*I*/d*V* peaks as the bias is varied within $\Delta_{CDW}$ (Figs. 4b and 5a). Note that this smooth energy–phase relation is reminiscent of the topological spectral flow of the edge modes. Figure 5a displays the energy–phase relation at the edge, demonstrating that the phase of the charge order at the gapless edge state vary gradually with energy solely for the bias voltages falling within the bulk energy gap ($\Delta_{CDW}$), resulting in a cumulative phase shift of π between the bulk valence and conduction band edges. Beyond this energy range, the

https://doi.org/10.1038/s41567-024-02469-1

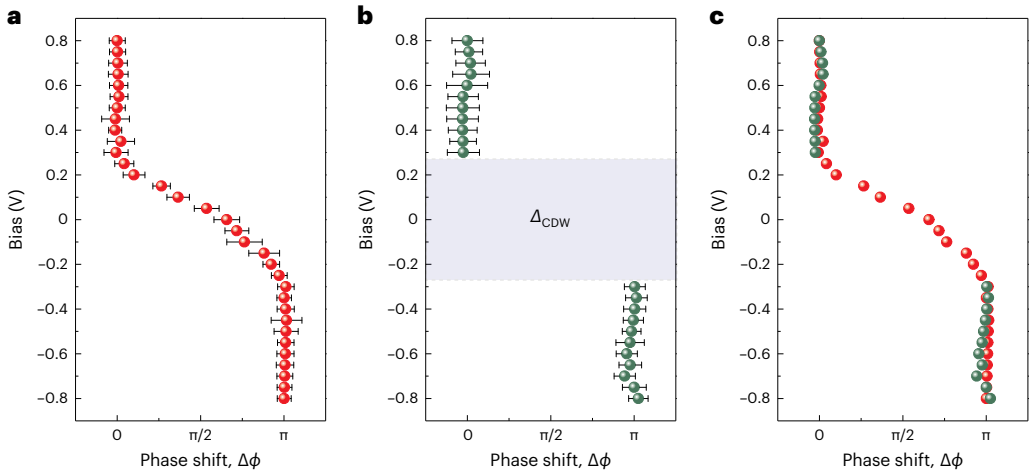


**Fig. 5 | Gapless edge mode connecting the gapped bulk (and surface) conduction and valence bands in energy and phase. a**, The deduced phase shift $\Delta\phi = \phi - \phi_{V=0.8V}$ of the edge d*I*/d*V* oscillations (obtained from the fit marked with red curves in Fig. 4b) akin to what is shown in Fig. 4b, plotted as a function of bias. As also visualized through the shift of the peak locations with varying bias in Fig. 4b, the phase shifts with energy solely for the bias voltages falling within the bulk energy gap ($\Delta_{CDW}$), resulting in a cumulative phase shift of π between the bulk valence and conduction band edges. Beyond this energy range, the phase remains constant within the bulk conduction or valence bands. **b**, The deduced phase shift $\Delta\phi = \phi - \phi_{V=0.8V}$ of the surface d*I*/d*V* oscillations (obtained from the fit marked with green curves), akin to what is shown in Fig. 4d, plotted as a function of bias. There are no data points within $\Delta_{CDW}$ due to the absence of a discernible bulk d*I*/d*V* signal at bias voltages falling within $\Delta_{CDW}$, characteristic of an insulating bulk gap. As visualized through tracking the peak locations with changing bias in Fig. 4d, the phase does not change within both the conduction and valence bands as a function of energy, yet there is a π phase shift between d*I*/d*V* oscillations acquired at the conduction and valence bands, creating a sharp π phase gap, present in conjunction with $\Delta_{CDW}$. **c**, Energy versus phase plots of the edge and the bulk in **a** and **b**, respectively, plotted together. The plot highlights the presence of a gapless edge state connecting the gapped (by $\Delta_{CDW}$ in energy and π in phase) bulk conduction and valence bands in energy and phase, bearing a resemblance to the topological spectral flow of the boundary modes. Data points in **a** and **b** are presented as ($\phi \pm \delta\phi$), where $\phi$ and $\delta\phi$ denote the optimal fitting parameter and 95% confidence interval of the fitting parameter, respectively.

phase remains constant within the bulk conduction or valence bands. When investigating the d*I*/d*V* line profiles along the same direction as in Fig. 4d, but away from the edge, we encounter d*I*/d*V* oscillations sharing the identical $(1.43 \pm 0.07)\lambda_{CDW}$ periodicity (Fig. 4d). Two critical aspects stand out in the data of Fig. 4d. Firstly, there are no data points within $\Delta_{CDW}$ owing to the absence of a discernible bulk d*I*/d*V* signal at bias voltages falling within $\Delta_{CDW}$, characteristic of an insulating bulk gap. Secondly, the phase remains constant within the conduction (or valence) band as a function of energy, yet there is a π phase difference between d*I*/d*V* oscillations at the conduction and valence bands, creating a sharp π phase gap in conjunction with $\Delta_{CDW}$ (illustrated in Fig. 5b). Notably, the π phase difference in the charge order between the bulk conduction and valence bands can also be inferred from the data in Fig. 1h,j. Lastly, Fig. 5c portrays the energy–phase relation of both the edge and bulk, juxtaposed to illuminate a crucial finding from our experiments. Specifically, it illustrates that the edge state—being gapless in both energy and phase—connects the bulk conduction and valence bands that are gapped by $\Delta_{CDW}$ (π) in energy (phase). This parallels the manner in which gapless topological boundary modes connect the gapped bulk bands in terms of energy and momentum magnitude. Such a linkage between the edge state and the underlying bulk charge order gap represents an unprecedented occurrence within the realm of wide-ranging charge density wave systems—consider, for instance, the case of $TaTe_4$, where an edge state was identified[56], though no definitive association between the edge state and the charge order was established.

It is tempting to interpret the underlying quantum state of the charge density wave insulator phase in $Ta_2Se_8I$ as a weak topological insulator composed of a stacking of two-dimensional quantum spin Hall states, with a stacking direction (equal to the vector of weak indices) perpendicular to the measured surface. However, theoretical arguments suggest that the vector of weak indices should be parallel to the ordering vector of the charge density wave[57], which is incompatible with our experimental observation. Another possibility is to have a gapped surface (and an edge state therein) due to surface reconstruction that can dimerize the pair of surface Dirac cones by breaking translation. However, the observed Bragg peaks (Fig. 1g and Supplementary Fig. 2b) are consistent with the ones that have been obtained with other bulk-sensitive techniques[23–29], showing no sign of additional surface reconstruction, thus contradicting this scenario. Therefore, while pointing to a topological nature of the observed edge state linked to the charge density wave phase, our experiments invite future theoretical works to understand whether it is related to the Weyl semimetal nature of the high-temperature phase.

To better understand the properties of the observed edge states and elucidate the essential physics, we construct a tight-binding model based on the nearly square iodine lattice and consider the charge density wave as a periodic potential in a sinusoidal form. Furthermore, we consider the system in a square geometry with the edges in the diagonal directions (~45° with respect to the square iodine lattice). In the absence of charge density wave, the system is gapless. The charge density wave opens sizable bulk gaps at low energies of the system with an oscillation pattern, which is consistent with the bulk d*I*/d*V* spectrum (Supplementary Fig. 9c,d). Strikingly, within the bulk gap, we find edge states that are exponentially localized at the edges. Moreover, by choosing appropriate parameters, we can obtain a bulk gap of size ~550 meV and, accordingly, a localization length $r_0 \approx 1.3$ nm of the edge states (Supplementary Fig. 9e,f). The localization length becomes longer as we decrease the bulk gap. The edge states exhibit a pronounced oscillation with a period $\sqrt{2}\lambda_{CDW}$ along the edge. Furthermore, the peak positions of the edge states along the edge shift for different biases, indicating an energy dispersion as a function of position[58]. These results are also in good agreement with our experimental observations. To understand the origin of the edge states, we analyse the decoupled wire limit where the hopping in one direction vanishes (Supplementary Fig. 10). In this limit, all wires are the same with identical charge density

wave phases and strengths. They exhibit topological bulk gaps, which are characterized by non-zero topological numbers, and consequently in-gap edge states under open boundary conditions. As we reduce the hopping strength in one direction to zero, the bulk gaps induced by the charge density wave remain open. This indicates that the topological insulating phase of our square lattice model is continuously connected to that of the decoupled wire limit. Thus, the edge states share the same topological origin and are characterized by the same topological numbers. We provide the details and more discussions of the model calculations in Supplementary Information. While more detailed, three-dimensional ab initio calculations are required to fully capture the topological properties of the charge density wave phase in $Ta_2Se_8I$, our two-dimensional effective model, built upon the surface square lattice of I atoms, suggests a feasible mechanism for the emergence of the edge state. It is essential to note, however, that conducting these ab initio calculations is currently highly computationally demanding due to the large charge density wave wavelength in this material.

The impact of our results is threefold. First, we visualize an in-gap edge state in $Ta_2Se_8I$ within the charge density wave gap. Going beyond the existing theories and the axion insulator interpretation of the charge density wave phase in $Ta_2Se_8I$, it indicates that the charge density wave state possibly contains a different, unique topology. Second, we find that the edge state is robust and persists up to $T_{CDW}$ (~260 K) before disappearing quickly above $T_{CDW}$. Additionally, we show a correlation between the decay length of the edge state and the strength of the charge order, as reflected in the increase of the decay length with the diminishing charge order gap. Remarkably, while the edge d$I$/d$V$ spectra exhibit oscillations with a periodicity closely matching the charge density wave period projected along the edge, the phase of these oscillations undergoes a π shift from the conduction band edge to the valence band edge. This phase shift of the gapless edge state connects the gapped bulk conduction and valence bands in both energy and phase, akin to a topological bulk–boundary connectivity in energy and momentum magnitude, albeit distinct in its phenomenology. Although tunnelling spectroscopy experiments alone cannot provide conclusive evidence of the topological nature of the edge states, these exotic behaviours collectively suggest the presence of a topologically non-trivial state, as supported by our theoretical analysis. Lastly, the charge density wave gap size surpasses the predictions from weakly coupled mean-field theory, suggesting a potential strong coupling nature, thus opening a new avenue for investigating the interplay between charge order, strong coupling and topology.

## Online content

Any methods, additional references, Nature Portfolio reporting summaries, source data, extended data, supplementary information, acknowledgements, peer review information; details of author contributions and competing interests; and statements of data and code availability are available at https://doi.org/10.1038/s41567-024-02469-1.

## References


1. Hasan, M. Z. & Kane, C. L. Colloquium: topological insulators. *Rev. Mod. Phys.* **82**, 3045–3067 (2010).
2. Yin, J. X., Pan, S. H. & Hasan, M. Z. Probing topological quantum matter with scanning tunneling microscopy. *Nat. Rev. Phys.* **3**, 249–263 (2021).
3. Hasan, M. Z. et al. Weyl, Dirac and high-fold chiral fermions in topological quantum matter. *Nat. Rev. Mater.* **6**, 784–803 (2021).
4. Nenno, D. M. et al. Axion physics in condensed-matter systems. *Nat. Rev. Phys.* **2**, 682–696 (2020).
5. Gooth, J. et al. Axionic charge-density wave in the Weyl semimetal $(TaSe_4)_2I$. *Nature* **575**, 315–319 (2019).
6. Allen, M. et al. Visualization of an axion insulating state at the transition between 2 chiral quantum anomalous Hall states. *Proc. Natl Acad. Sci. USA* **116**, 14511–14515 (2019).
7. Li, R., Wang, J., Qi, X.-L. & Zhang, S.-C. Dynamical axion field in topological magnetic insulators. *Nat. Phys.* **6**, 284–288 (2010).
8. Mogi, M. et al. A magnetic heterostructure of topological insulators as a candidate for an axion insulator. *Nat. Mater.* **16**, 516–521 (2017).
9. Liu, C. et al. Robust axion insulator and Chern insulator phases in a two-dimensional antiferromagnetic topological insulator. *Nat. Mater.* **19**, 522–527 (2020).
10. Zhang, D. et al. Topological axion states in magnetic insulator $MnBi_2Te_4$ with the quantized magnetoelectric effect. *Phys. Rev. Lett.* **122**, 206401 (2019).
11. Li, X.-P. et al. Type-III Weyl semimetals: $(TaSe_4)_2I$. *Phys. Rev. B* **103**, L081402 (2021).
12. Fijalkowski, K. M. et al. Any axion insulator must be a bulk three-dimensional topological insulator. *Phys. Rev. B* **103**, 235111 (2021).
13. Chiu, W.-C. et al. Causal structure of interacting Weyl fermions in condensed matter systems. *Nat. Commun.* **14**, 2228 (2023).
14. Shi, W. et al. A charge-density-wave topological semimetal. *Nat. Phys.* **17**, 381–387 (2021).
15. Qi, X.-L., Hughes, T. L. & Zhang, S.-C. Topological field theory of time-reversal invariant insulators. *Phys. Rev. B* **78**, 195424 (2008).
16. Essin, A. M., Moore, J. E. & Vanderbilt, D. Magnetoelectric polarizability and axion electrodynamics in crystalline insulators. *Phys. Rev. Lett.* **102**, 146805 (2009).
17. Malashevich, A., Souza, I., Coh, S. & Vanderbilt, D. Theory of orbital magnetoelectric response. *N. J. Phys.* **12**, 053032 (2010).
18. Sinchenko, A. A., Ballou, R., Lorenzo, J. E., Grenet, T. H. & Monceau, P. Does $(TaSe_4)_2I$ really harbor an axionic charge density wave? *Appl. Phys. Lett.* **120**, 063102 (2022).
19. Mitsuishi, N. et al. Switching of band inversion and topological surface states by charge density wave. *Nat. Commun.* **11**, 2466 (2020).
20. Yi, H. et al. Surface charge induced Dirac band splitting in a charge density wave material $(TaSe_4)_2I$. *Phys. Rev. Res.* **3**, 013271 (2021).
21. Huang, Z. et al. Absence of in-gap modes in charge density wave edge dislocations of the Weyl semimetal $(TaSe_4)_2I$. *Phys. Rev. B* **104**, 205138 (2021).
22. Aketagawa, M. & Takada, K. Correction of distorted STM image by using a regular crystalline lattice and 2D FFT. *Nanotechnology* **6**, 105 (1995).
23. Lee, K. B., Davidov, D. & Heeger, A. J. X-ray-diffraction study of the CDW phase in $(TaSe_4)_2I$-determination of the CDW modulation amplitude. *Solid State Commun.* **54**, 673–677 (1985).
24. Requardt, H., Kalning, M., Burandt, B., Press, W. & Currat, R. Critical x-ray scattering at the Peierls transition in the quasi-one-dimensional system $(TaSe_4)_2I$. *J. Phys. Condens. Matter* **8**, 2327 (1996).
25. Smaalen, S., Lam, E. J. & Ludecke, J. Structure of the charge-density-wave in $(TaSe_4)_2I$. *J. Phys. Condens. Matter* **13**, 9923 (2001).
26. Fujishita, H., Sato, M. & Hoshino, S. Incommensurate superlattice reflections in quasi-one-dimensional conductors, $(TaSe_4)_2I$ and $(NbSe_4)_2I$. *Solid State Commun.* **49**, 313–316 (1984).
27. Favre-Nicolin, V. et al. Structural evidence for Ta-tetramerization displacements in the charge density-wave compound $(TaSe_4)_2I$ from x-ray anomalous diffraction. *Phys. Rev. Lett.* **87**, 015502 (2001).
28. Fujishita, H., Shapiro, S. M., Sato, M. & Hoshino, S. A neutron-scattering study of the quasi-one-dimensional conductor $(TaSe_4)_2I$. *J. Phys. C: Solid State Phys.* **19**, 3049 (1986).
29. Lorenzo, J. E. et al. A neutron scattering study of the quasi-one-dimensional conductor $(TaSe_4)_2I$. *J. Phys. Condens. Matter* **10**, 5039–5068 (1998).

30. Li, G. et al. Chirality locking charge density waves in a chiral crystal. *Nat. Commun.* **13**, 2914 (2022).
31. Stoltz, D. et al. Tunneling evidence for spatial location of the charge-density-wave induced band splitting in 1*T*-$TaSe_2$. *Phys. Rev. B* **76**, 073410 (2007).
32. Mallet, P. et al. Contrast reversal of the charge density wave STM image in purple potassium molybdenum bronze $K_{0.9}Mo_6O_{17}$. *Phys. Rev. B* **60**, 2122 (1999).
33. Tournier-Colletta, C. et al. Electronic instability in a zero-gap semiconductor: the charge density wave in $(TaSe_4)_2I$. *Phys. Rev. Lett.* **110**, 236401 (2013).
34. Grüner, G. The dynamics of charge-density waves. *Rev. Mod. Phys.* **60**, 1129 (1988).
35. Flicker, F. & van Wezel, J. Charge order from orbital-dependent coupling evidenced by $NbSe_2$. *Nat. Commun.* **6**, 7034 (2015).
36. Varma, C. M. & Simons, A. L. Strong-coupling theory of charge-density-wave transitions. *Phys. Rev. Lett.* **51**, 138 (1983).
37. Zhang, Y. et al. First-principles study of the low-temperature charge density wave phase in the quasi-one-dimensional Weyl chiral compound $(TaSe_4)_2I$. *Phys. Rev. B* **101**, 174106 (2020).
38. Wang, Z. et al. Electronic nature of chiral charge order in the kagome superconductor $CsV_3Sb_5$. *Phys. Rev. B* **104**, 075148 (2021).
39. Stühler, R. et al. Tomonaga–Luttinger liquid in the edge channels of a quantum spin Hall insulator. *Nat. Phys.* **16**, 47–51 (2020).
40. Kane, C. L. & Mele, E. J. $Z_2$ topological order and the quantum spin Hall effect. *Phys. Rev. Lett.* **95**, 146802 (2005).
41. Bernevig, B. A. & Zhang, S.-C. Quantum spin Hall effect. *Phys. Rev. Lett.* **96**, 106802 (2006).
42. Bernevig, B. A., Hughes, T. L. & Zhang, S.-C. Quantum spin Hall effect and topological phase transition in HgTe quantum wells. *Science* **314**, 1757–1761 (2006).
43. König, M. et al. Quantum spin Hall insulator state in HgTe quantum wells. *Science* **318**, 766–770 (2007).
44. Yin, J. X. et al. Quantum-limit Chern topological magnetism in $TbMn_6Sn_6$. *Nature* **583**, 533–536 (2020).
45. Shumiya, N. et al. Evidence of a room-temperature quantum spin Hall edge state in a higher-order topological insulator. *Nat. Mater.* **21**, 1111–1115 (2022).
46. Drozdov, I. K. et al. One-dimensional topological edge states of bismuth bilayers. *Nat. Phys.* **10**, 664–669 (2014).
47. Tang, S. et al. Quantum spin Hall state in monolayer 1T′-$WTe_2$. *Nat. Phys.* **13**, 683–687 (2017).
48. Wu, R. et al. Evidence for topological edge states in a large energy gap near the step edges on the surface of $ZrTe_5$. *Phys. Rev. X* **6**, 021017 (2016).
49. Li, X.-B. et al. Experimental observation of topological edge states at the surface step edge of the topological insulator $ZrTe_5$. *Phys. Rev. Lett.* **116**, 176803 (2016).
50. Wang, Z. et al. Topological edge states in a high-temperature superconductor FeSe/$SrTiO_3$(001) film. *Nat. Mater.* **15**, 968–973 (2016).
51. Sessi, P. et al. Robust spin-polarized midgap states at step edges of topological crystalline insulators. *Science* **354**, 1269–1273 (2016).
52. Peng, L. et al. Observation of topological states residing at step edges of $WTe_2$. *Nat. Commun.* **8**, 659 (2017).
53. Liu, S. et al. Experimental observation of conductive edge states in weak topological insulator candidate $HfTe_5$. *APL Mater.* **6**, 121111 (2018).
54. Ugeda, M. M. et al. Observation of topologically protected states at crystalline phase boundaries in single-layer $WSe_2$. *Nat. Commun.* **9**, 3401 (2018).
55. Reis, F. et al. Bismuthene on a SiC substrate: a candidate for a high-temperature quantum spin Hall material. *Science* **357**, 287–290 (2017).
56. Zhang, X. et al. Eightfold fermionic excitation in a charge density wave compound. *Phys. Rev. B* **102**, 035125 (2020).
57. Wieder, B. J., Lin, K.-S. & Bradlyn, B. Axionic band topology in inversion-symmetric Weyl-charge-density waves. *Phys. Rev. Res.* **2**, 042010(R) (2020).
58. Zhang, S.-B. et al. Emergent edge modes in shifted quasi-one-dimensional charge density waves. *Phys. Rev. Lett.* **130**, 106203 (2023).
59. Chang, G. et al. Topological quantum properties of chiral crystals. *Nat. Mater.* **17**, 978–985 (2018).

## Methods

### $Ta_2Se_8I$ single-crystal growth and characterization

Tantalum powder (−325 mesh, 99.97% metals basis; Puratronic), iodine lump (ultradry, 99.999% metals basis) and selenium powder (−200 mesh, 99.999% metals basis) were purchased from Alfa Aesar and used for synthesis without further purification. Single crystals of $Ta_2Se_8I$ were grown using a chemical vapour transport method with Ta, Se and I as starting materials. Ta, Se and I were taken in a 2:8:1 composition ratio and sealed in an evacuated quartz tube. The ampoule was placed into a pre-heated dual-zone tube furnace with a temperature gradient of 500 °C to 400 °C and the educts in the hot zone for 2 weeks. After the growth period, a few-millimetre-long needle shape (with an aspect ratio of approximately 10) crystals had formed in the cold zone.

We conducted structural analysis on the cleaved $Ta_2Se_8I$ sample surface using electron diffraction measurements. In Supplementary Fig. 1b, we display the scanning electron microscopy image of the thin lamella, which was obtained through focused ion beam cutting from the cleaved surface that was required for performing the electron diffraction experiments. Supplementary Fig. 1c provides the electron diffraction pattern acquired at $T = 290$ K. Our electron diffraction analysis confirms that the cleaved surface corresponds to the (110) plane.

### Scanning tunnelling microscopy

Single crystals were cleaved mechanically in situ in ultrahigh vacuum conditions ($<5 \times 10^{-10}$ mbar) and then immediately inserted into the microscope head. The tunnelling junction set-up parameters for the topography and spectroscopy measurements are noted in the figure captions. Topographic images in this work were taken in the constant current mode. Tunnelling conductance spectra were obtained with a commercial W tip using the standard lock-in amplifier technique with a lock-in amplifier frequency of 977.77 Hz. For variable temperature measurements, we first withdrew the tip from the sample and then raised the temperature and stabilized the temperature for 12 h, after which we reapproached the tip to the sample to perform tunnelling experiments.

### STEM sample preparation and imaging

Thin lamellae were prepared by focus ion beam cutting using a Helios NanoLab G3 UC dual-beam focused ion beam and scanning electron microscope system. Sample thinning was accomplished by gently polishing the sample using a 2 kV $Ga^+$ ion beam to minimize surface damage caused by the ion beam. Conventional transmission electron microscope imaging and atomic resolution high-angle annular dark-field STEM imaging were performed on a Titan Cubed Themis 300 double Cs-corrected scanning/transmission electron microscope, operated at 300 kV.

### Angle-resolved photoemission spectroscopy measurement

The angle-resolved photoemission spectroscopy measurement was performed at SIS beamline of Swiss Light Source, Switzerland. The energy and momentum resolution were below 20 meV and 0.02 $Å^{-1}$, respectively. The Fermi level was determined by measuring a polycrystalline gold that was electrically grounded with the measured sample.

## Data availability

All data needed to evaluate the conclusions in the paper are present in the paper. Additional data are available from the corresponding authors upon reasonable request. Source data are provided with this paper.

## Acknowledgements

The M.Z.H. group acknowledges primary support from the US Department of Energy, Office of Science, National Quantum Information Science Research Centers, Quantum Science Center (at ORNL) and Princeton University; scanning tunneling microscopy instrumentation support from the Gordon and Betty Moore Foundation (GBMF9461) and the theory work; and support from the US DOE under the Basic Energy Sciences programme (grant number DOE/BES DE-FG-02-05ER46200) for the theory and sample characterization work including photoemission spectroscopy. T.N. acknowledges supports from the European Union's Horizon 2020 research and innovation programme (ERC-StG-Neupert-757867-PARATOP) and from the Swiss National Science Foundation through a Consolidator Grant (iTQC, TMCG-2_213805). Work at Nanyang Technological University was supported by the National Research Foundation, Singapore, under its Fellowship Award (NRF-NRFF13-2021-0010), the Agency for Science, Technology and Research (A*STAR) under its Manufacturing, Trade and Connectivity (MTC) Individual Research Grant (IRG) (Grant No.: M23M6c0100), and the Nanyang Assistant Professorship grant (NTU-SUG). Crystal growth at Beijing Institute of Technology is supported by National Science Foundation of China (NSFC) (grant nos 92065109, 12321004 and 12234003), the National Key R&D Program of China (grant nos 2020YFA0308800 and 2022YFA1403400) and the Beijing Natural Science Foundation (grant no. Z210006). Z.W. thanks the Analysis and Testing Center at BIT for assistance through facility support. S.-B.Z. is supported by the Innovation Program for Quantum Science and Technology (grant no. 2021ZD0302800) and the Anhui Initiative in Quantum Information Technologies (grant no. AHY170000). Crystal growth at Max Planck Institute for Chemical Physics of Solids is funded by European Research Council (ERC) advanced grant no. 742068 ('TOPMAT'), the Deutsche Forschungsgemeinschaft (DFG) under SFB 1143 (project no. 247310070) and the Würzburg-Dresden Cluster of Excellence on Complexity and Topology in Quantum Matter – ct.qmat (EXC 2147, project no. 39085490). G. Cheng and N.Y. acknowledge the use of Princeton's Imaging and Analysis Center, which is partially supported by the Princeton Center for Complex Materials, a National Science Foundation (NSF)-MRSEC programme (DMR-2011750). X.L. acknowledges support from the National Key R&D Program of China (grant no. 2022YFA1403700).

## Author contributions

STM experiments were performed by M.L. and M.S.H. in consultation with M.Z.H. Crystal growth was carried out by S.N.G., N.K., C.S., Z.W. and Y.L under supervision of Y.Y. and C.F. Transmission electron microscopy measurements were performed by G.C. and N.Y. ARPES experiments were performed by Z.-J.C. in consultation with M.S.H. and M.Z.H. Theoretical modelling and calculations uncovering the underlying topology of the boundary mode were carried out by S.-B.Z. and X.L. under supervision of T.N. Writing of the manuscript and figure production were undertaken by M.S.H., M.L., S.-B.Z., T.N., Z.-J.C. and M.Z.H. All the authors contributed to the discussion of the results, interpretation and conclusion.

## Competing interests

The authors declare no competing interests.

## Additional information

**Supplementary information** The online version contains supplementary material available at https://doi.org/10.1038/s41567-024-02469-1.

**Correspondence and requests for materials** should be addressed to Md Shafayat Hossain or M. Zahid Hasan.

**Peer review information** *Nature Physics* thanks Amit Agarwal, Somesh Ganguli and the other, anonymous, reviewer(s) for their contribution to the peer review of this work.